Aerothermodynamics and TPS Sizing of Skip Re-Entry and Aerocapture Vehicles

A project present to
The Faculty of the Department of Aerospace Engineering
San Jose State University

in partial fulfillment of the requirements for the degree
Master of Science in Aerospace Engineering

By

Max Jeng

December, 2017

approved by

Dr. Periklis Papadopoulos
Faculty Advisor

San José State
UNIVERSITY

The Designated Project Advisor Approves the Thesis Titled

AEROTHERMODYNAMICS AND TPS SIZING OF SKIP RE-ENTRY AND AEROCAPTURE
VEHICLES

by

Max Jeng

APPROVED FOR THE DEPARTMENT OF AEROSPACE ENGINEERING

SAN JOSÉ STATE UNIVERSITY

December 2017

Dr. Periklis Papadopoulos   Department of Aerospace Engineering   Advisor

ABSTRACT

AEROTHERMODYNAMICS AND TPS SIZING OF SKIP RE-ENTRY AND AEROCAPTURE VEHICLES

by Max Jeng

A study was conducted to analyze the aerothermal effects of a spacecraft during its aerocapture and skip re-entry maneuvers. The program FIATv3 was used to calculate the stagnation point heat flux of a skip re-entry vehicle. An investigation that utilized a modified version of the Apollo Command Module vehicle was referenced for the aerothermodynamics of vehicles placed in Earth parking orbits through aerocapturing. The combined aerothermal results were compared with that of the Stardust sample return capsule during its direct Earth re-entry. The goal of this project is to determine the advantageous effects exhibited by the combined aerocapture to skip re-entry maneuver over a direct entry maneuver.

ACKNOWLEDGEMENTS

Table of Contents

Nomenclature

BLIMP	= Boundary Layer Integral Matrix Procedure	
CFD	= Computation Fluid Dynamics	
CRB	= Cramer-Rao Lower Bound	
DPLR	= Data Parallel Line Relaxation	
FIAT	= Fully Implicit Ablation and Thermal Response Program	
KATS	= Kentucky Aerodynamic and Thermoresponse System	
MAT	= Multicomponent Ablation Thermochemistry	
PICA	= Phenolic Impregnated Carbon Ablator	
POST	= Program to Optimize Simulated Trajectories	
SRC	= Sample Return Capsule	
TACOT	= Theoretical Ablative Composite for Open Testing	
TITAN	= Two-Dimensional Implicit Thermal Response and Ablation	
TPS	= Thermal Protection System	

Symbols

$T_{\Re}$	= Wall temperature at radiation equilibrium	K
$\acute{q}_{conv}$	= Convective heat flux	W/m^2
$\acute{q}_{rad}$	= Radiative heat flux	W/m^2
σ	= Stephan-Boltzmann constant	W/(m^2·K^4)
ε	= Material emissivity	
$\acute{q}_{sc}$	= Stagnation point convective heat flux	W/m^2
p_s	= Boundary layer pressure	atm
$r_{eq,b}$	= Equivalent body radius	m
$N_{Pr,w}$	= Prandtl number at the wall	
M_e	= Molecular weight at boundary layer	
R	= Universal gas constant	J/kmole·K
T_e	= Temperature at boundary layer external edge	K
M_o	= Molecular weight of initial composition	
$\mu_{o,e}$	= Viscosity of initial composition at boundary layer	N·s/m^2
h_s	= Enthalpy at external edge of boundary layer	J/mole
h_w	= Enthalpy at the wall	J/mole
$\beta_{2,w}$	= Constant at the wall, dependent on molecular weight	

M_w	= Molecular weight at the wall	
$N_{i,w}$	= Lewis number at the wall	
F_i	= Diffusion factor	
z_i	= Constant dependent on molecular weight, diffusion factor, velocity gradient	
ρ	= Air density	kg/m³
ϕ	= Porosity	
Γ	= Resin volume fraction	
ρ_A	= Density of organic resin A	kg/m³
ρ_B	= Density of organic resin B	kg/m³
ρ_C	= Density of char material	kg/m³
A	= Pre-exponential constant	
ρ_v	= Density of virgin material	kg/m³
ψ	= Decomposition reaction order	
E	= Activation energy	J
T	= Surface temperature	K
Φ	= Relative volume parameter	
Φ_c	= Ratio of char-to-virgin volume	
c_p	= Material specific heat	J/g·K
x	= Mass fraction of virgin material	
C_H	= Stanton number for heat transfer	
C_M	= Stanton number for mass transfer	
$\rho_e u_e C_H$	= Heat transfer coefficient	W/m²·K
H_r	= Recovery enthalpy	J/mole
m_c	= Char mass	kg
h_c	= Char enthalpy	J/mole
m_g	= Pyrolysis gas mass	kg
h_g	= Pyrolysis gas enthalpy	J/mole
α_w	= Wall surface absorptance	

$\acute{s}$	= Ablation rate	kg/m²·s
h_f	= Failing species enthalpy	J/mole
T_w	= Wall temperature	K
T_∞	= Freestream temperature	K
$\acute{q}_{cond}$	= Conductive heat flux	W/m²
B'	= Non-dimensional mass flow rate	kg/s
$C_{H,1}$	= Stanton number for heat transfer, unblown value	
λ	= Blowing reduction parameter	
B'_1	= Non-dimensional mass flow rate, unblown value	kg/s
ε_w	= Wall emissivity	
h	= Enthalpy	J/mole

1.0 Introduction

The recent increase of public interest in the exploration of moons and planets in the solar system has driven space agencies and private companies to begin planning for such operations. The conventional method for placing vehicles into parking or transfer orbits requires the use of rocket boosters for increasing or decreasing the vehicle's velocity. This method demands a large proportion of the spacecraft mass be reserved for rocket fuel. However, a spacecraft can utilize aerocapturing maneuvers, where the atmospheric drag and the planet's gravitational forces decrease the vehicle's velocity and guide it into a parking orbit, to reduce the overall mission costs. Aerobraking increases the amount of payload that can be carried on each mission by reducing the amount of fuel needed for retrograde rockets. The Aeroassist Flight Experiment was a mission designed to study the aerodynamics and aerothermodynamics of a spacecraft transferring from geosynchronous Earth orbit to low Earth orbit through aerocapturing maneuvers [2]. Although the mission was eventually cancelled, the progress made during the design and testing phases yielded valuable data for high-velocity and low-density environment operations.

Skip re-entry allows returning vehicles traveling at hyper-velocities to extend the duration of its re-entry which permits the immense thermal energy to dissipate at a more manageable rate. Skip re-entry also increases the down-range and cross-range potential of the vehicle. This maneuver is achieved by first "dipping" the vehicle into the planet's lower and denser atmosphere to reduce velocity before lifting back out of the atmosphere for readjustments in preparation for the final entry. The Apollo Command Module had the capabilities to perform the skip re-entry upon its return to Earth but instead performed a partial skip [3]. The vehicle lifted after the initial entry to avoid experiencing extreme heat loads but never fully left the atmosphere. The Russian Zond program that focused on testing their circumlunar capabilities did execute skip re-entries upon returning to Earth.

In contrast, the Stardust sample return capsule executed a conventional atmospheric entry and descended continuously through the atmosphere until landing. The SRC was initially slowed by an aeroshell followed by a series of parachutes. By the time the SRC had separated from the main spacecraft and entered the atmosphere, it was traveling at nearly 12.8 km/s, which was the fastest Earth re-entry velocity ever attained by a man-made object [4]. The SRC had experienced a deceleration of up to 34 Gs but the capsule and its payload remained intact. The heatshield received the brunt of the heat load and temperatures rose to above 2,900 $^{\circ}$C during its journey.

When the primary means of reducing a vehicle's velocity is through atmospheric drag, the ability of the vehicle's thermal protection system to withstand the extreme heat loads experienced is critical. The prolonged travel and the various approach angles through the atmosphere place a great demand on the vehicle's TPS.

The TPS of a spacecraft employs active protection using heaters and heat pipes and passive protection from radiators to various high-emissivity tiles and surface coatings. A TPS ensures crucial components of a spacecraft remain within the temperature limits of operation, so that the machines will continue to function for the duration of the mission and in some cases, be re-usable. A major concern of an entry vehicle's TPS is the heat shield. A heat shield is responsible for protecting the vehicle's structural integrity and the payload inside the vehicle from thermal damage. The heat shield is typically made of reinforced composites that, when heated by the extreme temperatures in the absence of oxygen, pyrolyzes and creates by-product gases. The pyrolysis gases move from the body of the vehicle toward the heated surfaces and into the

boundary layer, thus completing the transfer of energy from the solid to the gaseous. The chemical reactions between the pyrolysis gases and the boundary layer gases increase the total heat flux at the material surface. Ambient temperatures can reach up to several thousand degrees Celsius during the intense hypersonic entry phase. The sublimation of surface materials can cause the surface to recede. It is important for engineers to understand the chemical reactions of gases occurring at such high speeds and the ablative process surrounding the vehicle during its atmospheric entry so that an appropriate heat shield can be designed and implemented. Heat flux, the rate at which thermal energy is transferred between the environment and the material, dictate the amount of ablation and pyrolysis the material experiences, and thus is of great importance when designing the thickness of the heatshield.

2.0 Literature Review

2.1 Aerocapturing Maneuver Design

The aerocapturing maneuver of the Mars SRC, a subscaled Apollo Command Module shaped like a blunt-bodied gumdrop, was investigated using an experimental TPS design [1]. The Mars SRC is an unmanned return capsule meant to aerocapture and stay in parking orbits around Earth. The forward heatshield of the Mars SRC, known as the aerobrake, was 1.8 meters in diameter and was comprised of the AVCO-5026 covered with an aluminum skin [2]. The AVCO-5026 was the primary TPS material of the Apollo Command Module and was made using an epoxy novolac resin mixed with special additives. A shell-like honeycomb structure is bonded to the spacecraft before the resin is injected into the honeycomb cells. The Mars SRC was designed to be captured in a 500 km x 500 km orbit entering at 12 km/s around Earth. The minimum vehicle altitude was 68.9 km above Earth. Once the trajectories were identified, approximating a catalytic surface during maximum heat loads using an equilibrium flow heat distribution became possible. The convective stagnation heat flux and radiative heat flux for Earth entry were calculated using the Boundary Layer Integral Matrix Procedure computer program. The heat loads were calculated with regards to the chemically reacting laminar or turbulent boundary layer. The computations were valid for a partially catalytic wall in nonequilibrium flow or a fully catalytic wall in local thermodynamic equilibrium. BLIMP utilized an iteration program to determine the wall temperature at radiation equilibrium based on the sum of the convective and radiative heat flux.

$$T_{\Re} = \frac{\acute{q}_{conv} + \acute{q}_{rad}}{\sigma\varepsilon}$$

(2.1.1)

The AESOP-STAB thermal analysis program computed the minimum TPS weight for the ablative system present on the Mars SRC. Pyrolysis of the ablative material occurred in the reaction zone specified by the density and temperature limits. The results of this investigation, which will be further discussed in Section 5.0, demonstrated that utilizing atmospheric drag through aerobraking was more efficient than employing an exclusively propulsive system for parking orbit engagements.

2.2 Skip Re-entry

The amount of stress encountered by the vehicle and its occupants can be severe during an atmospheric entry. This is especially true for command modules that typically have low lift-to-

drag ratios which impede its ability to maneuver. The low lift-to-drag ratio decreases the range of the vehicle and forces it to traverse layers of dense atmosphere in a short period of time. An established solution is to utilize the skip re-entry method where the vehicle first enters the atmosphere to reduce its velocity but changes its trajectory to lift back out of the atmosphere. Corrections for velocity, down-range, and flight path angles are made during the skip phase before committing to the final entry and landing. It was determined during the Apollo missions that computations for the skip trajectory and final entry guidance commands must be made on-board so the precise flight conditions are known. However, limited on-board computational capabilities prevented the Apollo missions from ever executing the skip re-entry maneuvers with confidence.
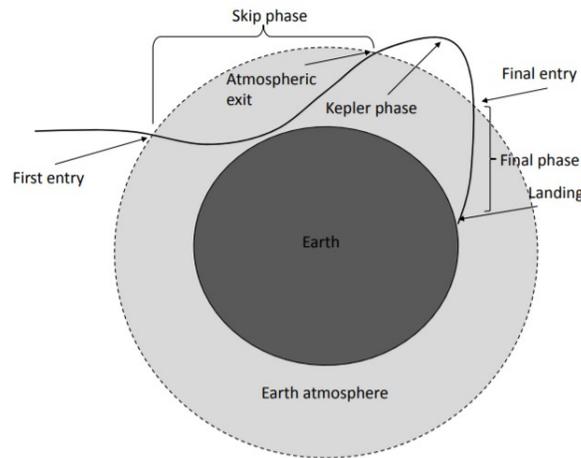
Figure 2.2.1 Skip re-entry trajectory

A trajectory planning and guidance for low lift-to-drag ratio vehicles using a numerical predictor-corrector method was formulated [3]. This technique guides the trajectory through modulation of the vehicle's bank angle, which is dependent on the down-range requirement and the location of the landing site. To ensure a precise landing prediction, three degree of freedom trajectory dynamics and dispersion simulations were computed repeatedly. The developed algorithm was compared with that of the Apollo missions and demonstrated significant improvements for trajectory design and guidance accuracy.

2.3 Stardust SRC

The Earth re-entry of the Stardust SRC in January 2006 generated great interests among groups of NASA researchers tasked with returning humans to the moon. One of the integral components in achieving that goal was the design of the Crew Exploration Vehicle, also known as the Orion spacecraft. Orion had to be able to withstand Earth re-entries at super-orbital velocities from trans-lunar trajectories. The blunt-body capsule and the predicted aerothermal environment on the Orion spacecraft are similar in scale to those of the Stardust SRC. Unfortunately, the SRC was not equipped with any sensors, therefore, no direct aerodynamic or aerothermodynamic measurements were made. The data and analysis presented by [4] were derived from three sources: radar signals during the descent stage, spectral resolution of the shock layer gases and the glowing SRC provided by airborne observations, and the recovered TPS of the return capsule. The aerothermodynamics of the SRC during re-entry will be provided and discussed in Section 5.0.
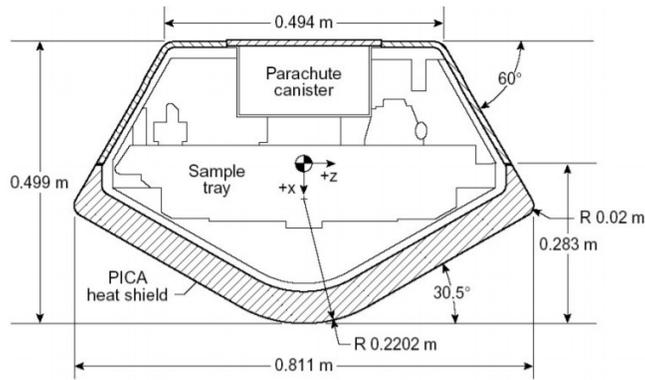
Figure 2.3.1 Stardust Sample Return Capsule

Built by the Lockheed Martin Space Systems Company, the SRC aeroshell was composed of a 60° truncated cone backshell and a 30° sphere-cone forebody heatshield. The baseline forebody material of the SRC was PICA, a lightweight ceramic ablator material developed at NASA Ames Research Center. The backshell was made using the Super Lightweight Ablator (SLA)-561V, a material that has been proven through its uses in most NASA missions to Mars (e.g. Pathfinder, Viking). The Stardust mission demanded its TPS keep the sensitive payload within the vehicle under 70 °C. In designing the TPS of the SRC, arc jet tests were performed to investigate the thermal and ablative responses of PICA under the predicted peak entry conditions to be encountered during the mission [5]. Sixteen PICA cylindrical test models of 2.54 cm and 5.08 cm diameters were examined for ablative performances. To compare thermal responses, another sixteen PICA models of 10.16 cm in diameter were tested at less intense atmospheric conditions. The arc jet test data were compared with computed estimations to improve and refine the simulation model for ablative and thermal response of PICA heat shields.

The recession rate of the material at the surface was deemed the best measure of ablative performance. The results of the two smaller models showed a clear trend of increasing recession rate with time. That may be due to the depletion of the phenolic resin which reduced the overall blowing effect by the pyrolysis gases and thus reduced the blockage of convective heating. The thermal responses of the 10.16 cm model are shown in Figure 2.3.2.
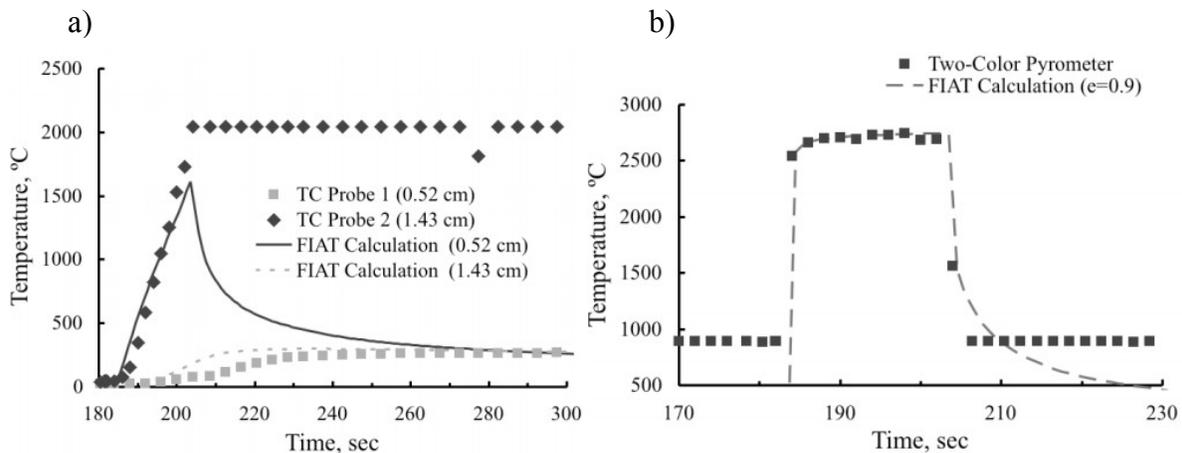
Figure 2.3.2 Comparison of experimental and calculated thermal response a) in-depth and b) at the surface

4

The temperatures experienced during testing were all well below the allowable maximum temperature specified for the mission. PICA was shown to be a reliable and effective material for modern and future high speed atmospheric travels.

2.4 3D Investigation on Charring Ablator

Weng and Martin aimed to model the Stardust SRC heatshield in three dimensions [6]. In addition, the authors conducted a study to explore the validity of modeling aerothermal phenomena around the ablative heatshield of an entry vehicle as a one-dimensional problem versus a three-dimensional problem. Specifically, data from the Stardust SRC were examined along with one-dimensional simulation results from other studies.

The material used for the heatshield simulation in this study was the Theoretical Ablative Composite for Open Testing. TACOT is based on and performs similarly to PICA. The Klinkenburg permeability model that accounts for the transverse isotropic transport behaviors of charring ablative materials was implemented to increase the accuracy of predictions. Kentucky Aerodynamic and Thermoresponse System was the material response module employed by the author for this study. KATS' governing equations contain a multi-component solid decomposition model, a time accurate gas momentum transport model, a mixture energy conservation, and a pyrolysis gas mass conservation model. A fixed Cartesian coordinate system along with a finite volume method were used for calculations.
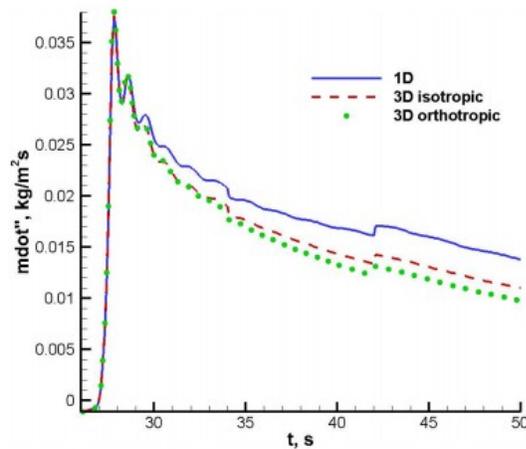
Figure 2.4.1 Stagnation blowing rates

Based on the results seen in Figure 2.4.1, the surface temperature and the heating rates between the one-dimensional and three-dimensional models appeared to be very similar. However, the interior temperatures of the material below the surface varied greatly from one-dimensional to three-dimensional models; by as much as 700 K. A possible explanation was that the pyrolysis gases created in the decomposition zone had a large enthalpy, and was able to heat up the material and raise the overall temperature. In conclusion, one-dimensional models are capable of estimating stagnation point temperatures but may fail to produce accurate data for in-depth material thermal response.

2.5 PICA Validation

Milos and Chen conducted a series of analyses to demonstrate the validity of the PICA heat shield and compared the results of computer simulation results with actual arc jet test data [7]. PICA was developed by NASA in the 1990's as a lightweight ceramic ablator of the future. To date, PICA has been the TPS material of several spacecraft, including the Mars Science Laboratory, the SpaceX Dragon spacecraft, and the Stardust SRC. PICA is a low density, rigid, and carbon fiber composite material impregnated with a phenolic resin. Figure 2.5.1 a) is the model used in recent arc jet testing. Figure 2.5.1 b) shows the effects of ablation. The PICA sample was tested for 200 seconds and recessed by 13 mm at the centerline. The heating on the sidewall was significant enough to cause recession. However, the ablated model was still relatively able to retain its original shape.

a)   b)
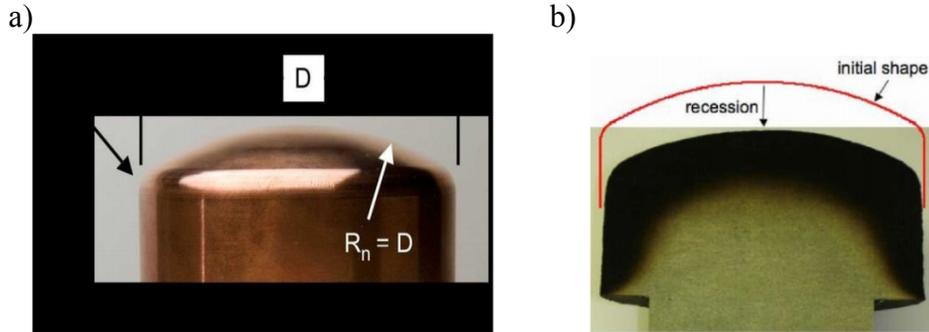
Figure 2.5.1 a) Model shape for testing and b) cross section of model after testing

The PICA model was put through experiments with 18 different testing conditions that varied the mixture ratio of air and Argon, exposure time, nozzle diameter of wind tunnel, and stagnation pressure. Figure 2.5.2 shows the stagnation conditions from experiments at both the Ames Research Center and Johnson Space Center. As the test conditions became harsher, the stagnation pressure and heat flux increased, which explains the apparent linear relationship between the two.
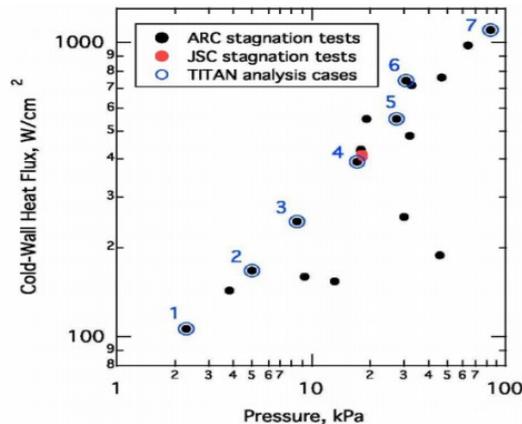
Figure 2.5.2 Cold-wall heat flux and stagnation pressure for various test conditions

The surface temperatures of the models were measured with two single-wavelength optical pyrometers and one dual-wavelength pyrometer. In-depth temperatures were measured at five to ten different locations with multiple bare-wire thermocouples.

Using programs like the Data Parallel Line Relaxation to solve time-dependent conservation equations, Two-dimensional Implicit Thermal response and AblatioN program (TITAN) and

FIAT to predict ablation, pyrolysis, and thermal conduction in one and two dimensions, Milos and Chen were able to confirm the experimental data with the results produced by TITAN and FIAT. Simulation results fell well within the uncertainty percentages for surface recession, heat flux at various locations, and thermal penetration. However, and as expected, the in-depth thermal analyses using a one-dimensional model proved to be insufficient, since the thermal response was greatly affected by multi-dimensional heat conduction. The two-dimensional models used by TITAN accurately predicted the in-depth thermal response. In conclusion, Milos and Chen were able to validate the effectiveness of PICA as a TPS material through numerous simulations and comparisons with test data.

2.6 Ablative TPS Sizing Tool

A computer tool that estimates the TPS sizing of an entry vehicle was created by Dec and Braun. The tool provides two options to calculate the sizing [8]. First, a high-fidelity ablation program that utilizes trajectory data to simulate the boundary conditions around the TPS. Second, the tool couples the estimation of heat shield recession with a one-dimensional finite-difference method that can calculate detailed thermal responses. This option makes use of data from material decomposition but is unable to account for transfer of pyrolysis gas energy through the ablation material. The stagnation-point convective heat was calculated using the Sutton-Graves convective heating relation. Having been verified by ground-based and flight tests, the Sutton-Graves relation was found to be accurate to within 5-10%. The stagnation-point radiative heating was represented by the Tauber-Sutton relation. The sum of the convective and radiative heat rates produced the total heat rate at each point along the trajectory. The total heat loads were calculated by integrating the heat rates over the path of the trajectory.

The sizing of the TPS was put through an iterative scheme known as the secant method where the initial estimate of the TPS thickness was used to calculate the thermal response while a second calculation used a thickness 0.1 cm greater than the initial thickness. If the two calculations produced similar bondline temperatures, then the initial thickness was reduced by half. The process repeated until the bondline temperature produced matched the given temperature to within 0.1 ℃.

To demonstrate the validity of the two options provided by the sizing tool, the results were compared with the Mars Pathfinder and Stardust missions of NASA. In comparison with the Mars Pathfinder, the second option was consistently more accurate in predicting the thickness of the heatshield at the stagnation point as well as the surface and bondline temperatures. Comparing with the Stardust mission, both options produced acceptable results within the margin of error. The first option produced better predictions for heat shield recessions and cases with ablation while the second option correlated well to cases without ablation. Again, this was explained by the fact that the second option did not account for the effects of energy absorption and convection of pyrolysis gases through the TPS material. Further studies were compared with the Apollo missions. The results showed that in high-density materials where negligible heat shield recession is expected, the second option typically produced more accurate results. However, as the density of the TPS material decreased and heat flux increased, a greater degree of ablation occurred and the first method was able to produce more reliable results.

2.7 FIAT

The Fully Implicit Ablation and Thermal response program developed by Milos and Chen of NASA simulates one-dimensional transient thermal energy transfer in multilayer TPS structures

that ablate and decompose [9]. Utilizing a fully implicit solution methodology so that a more desirable numerical stability can be achieved, FIAT couples the internal energy balance and decomposition equations with a surface energy balance and thermochemical ablation model. Depending on the type and thickness of the material, FIAT will generate a grid for each material ply. The top ply is stretched geometrically and has a finer resolution near the externally heated surface. Temperature, pressure, and density are assigned at the cell centers, and heat and mass fluxes are assigned at the cell intersections. The flow of pyrolysis gas is assumed to be quasi-steady and in the direction normal to the surface. Due to the non-Lagrangian motion of the grid during compression, the equations of the top plies are more complex.

Each execution of FIAT requires at least three and up to four input files which contain information of the ply and run parameters, the heating environment, the material properties, and optionally, the thermodynamics species. Once the program completes its execution, five output files containing information on the through-thickness profiles, pyrolysis and ablation quantities, temperature and heat flux at material interfaces, thermocouples and isotherms, and grid data will be produced. Depending on the thickness and type of material, FIAT will create a grid for each material ply, up to a maximum of 15 plies. The top-ply is geometrically stretched, contains small cells near the top surface, and the grid in the top ply is compressed in cases where recession occurs. The subsurface plies can contain stretched grids to account for the full ablation of the outer plies. The temperature, density, and pressure are defined at the cell centers while the heat and mass fluxes are defined at the cell interfaces. If the user specifies the maximum temperature limits of each subsurface interface and the maximum and minimum allowable thickness to use for the optimization of the material, FIAT can determine the minimum thickness of any ply within the material.

In the main input and environment input files, the following are required as user inputs:
analysis, three types of subsurface reactions were considered:
1. Freestream temperature
2. Total time and timestep
3. Number of plies
4. Type of material for each ply
5. Initial temperature of each ply
6. Initial thickness of each ply
7. Number of cells in each grid
8. Angle between through-the-thickness and normal surface directions
9. Type of atmosphere

The material input files will be left in their default states as those files were designed to be used but not edited by the user.

The following are generated in the output files by FIAT:
1. Sizing iteration history
2. Time dependent surface boundary conditions
3. Temperatures and heat fluxes at material interfaces with respect to time
4. Depth of pyrolysis and ablation quantities with respect to time
5. Surface mass flux with respect to time
6. Peak bondline temperatures
7. Recession of materials

8.   Surface Energy Balance terms and integrated values

FIAT was first developed in 1998 and has been consistently updated to improve user interface, sizing optimization, input/output file structures, grid generation, and overall accuracy of the program. The code was utilized by NASA for the Stardust, Mars 2001, and Mars Microprobe missions to conduct analyses on the aeroshell heat shields of the vehicles.

2.8 Charring Ablator Response

Rindal conducted an in-depth analysis of an ablation material that experienced subsurface coking and designed a model to represent mass, momentum, and energy transfer events in a charring and coking ablator [10]. A mathematical model systematically evaluated the effects of forward and reverse coking reactions while conserving chemical elements at the surface and in-depth. The assumption was made that a certain class of chemical reactions caused the transfer of carbon between the pyrolysis gases and the char layer. Coking reactions are considered as the thermal cracking of hydrocarbons which results in precipitation of carbon onto the char layer. For the analysis, three types of subsurface reactions were considered:

1.   The decomposition of three organic components to create the initial char and pyrolysis products
2.   The decomposition of the pyrolysis gas which results in carbon precipitation and char densification
3.   The chemical erosion of the subsurface char layer by the pyrolysis gases at higher temperatures

Forward and reverse coking reactions generally occur in the low and high temperature regions of the char layer, respectively. Coking reduces the permeability of the char layer and generates high pressure in-depth, which can result in excessive char stress and catastrophic failure of the char layer. Once the decomposition gases have been formed, they will travel through the permeable char layer toward the heated surface. An increase in gas temperature and decrease in pressure will push the initial decomposed gases through chemical reactions as they pass through the char layer. Three types of reactions were to be expected:

1.   Decomposition of the gas, thermal decomposition of hydrocarbons with high molecular weights, and dissociation of CO_2, H_2O, and H_2.
2.   Continuous decomposition of hydrocarbon that results in precipitation of carbon into the char layer and increased density of char buildup
3.   Chemical erosion of the char layer below the heated surface by gases, such as vaporization of carbon which can result in reduced char density

Rindal was able to identify the importance of subsurface coking reactions and formulated the charring and coking phenomena of ablation material into prediction models that became a part of the mathematical solver. The models showed noticeable impact by precipitated carbon on the overall thermal response of the ablation material and in the boundary layer.

2.9 Chemical Recombination in Boundary Layer

The aerothermodynamic analysis of a low-Earth orbit crew return vehicle during re-entry has been conducted [11]. Imprecise thermal response predictions in the past have been caused by inadequate knowledge of the real gas aerothermodynamics and the catalytic effects on the heat shield walls. It has been established that nonequilibrium finite rate chemistry and transport properties have a significant impact on the position and geometry of Mach and shock waves, which in turn affect the aerodynamics, trajectory, and thermal response of the vehicle. It was

found that the presence of dissociated gases could increase, by orders of magnitude, the heat load experienced by the heat shield. For example, the heat shield material could cause chemical recombination at the reattachment shock after the gases have passed through the bow shock ahead of the vehicle. The recombination reactions could more than double the heat shield surface heat flux.

To highlight the importance of real gas and catalytic effects in a spacecraft design, the authors performed two types of numerical simulations. The first simulation was done by the Entry Trajectory tool that provided a quick and reliable preliminary design analysis. The second simulation was done with CFD using a 3-D Navier-Stokes numerical computation that accounted for wall boundary conditions and real gas effects. To efficiently convert the large quantities of kinetic and potential energy of the vehicle into the heat energy of the surrounding flow field, the vehicle must have a blunt forebody and be traveling at a high angle of attack. However, these conditions promote the formation of detached bow shocks ahead of the vehicle. As the gas particles travel through the bow shock, the total freestream enthalpy can cause molecular dissociation and turn the flow into plasma. Recombination occurs when the dissociated atoms reach the body wall and form into molecules in the boundary layer or at the surface, and in the process, transfer the energy from recombination to the boundary layer or the surface. The magnitude and rate of heat transfer depend on the surface temperature and the chemical compositions of the gases and surface material.

The results produced were able to confirm that a comprehensive knowledge of the chemical flow field behavior is critical to the design of a vehicle TPS. A low-catalytic TPS material is extremely beneficial for reducing the possibility of recombination.

2.10 Cavities and Protuberances

Events like the hypersonic re-entry of space capsules are characterized by vehicles moving at extremely high velocities (10-15 km/s) interacting with the dense atmosphere, creating huge amounts of energy transfer between the vehicle and the gas particles in its surrounding flow field. During those circumstances, any structural irregularities on the surface of the vehicle can result in catastrophe. The Apollo Command Module and the Genesis SRC both had a number of cavities and protuberances as part of their structural design. Experimental tests demonstrated severe local heating at the cavities and protuberances which created concerns about the thermal stresses at the locations of the irregularities being sufficient enough to cause local structural failure of the heatshield. Cavities could also form from the penetration of debris impacts during launch or while out in space, trailing behind comets for sample collection. The authors wished to study the impacts that local cavities and protuberances have on the performance of heat shields [12]. A numerical flow simulation for typical entry conditions was employed to compute the local thermal responses of various physical irregularities on the surface. Predictions for surface heating during atmospheric entry were calculated from laminar, non-equilibrium, axisymmetric Navier-Stokes flow field equations.

To contrast the effects cavities, a Genesis heat shield geometry with and without surface cavities were tested. The experimental vehicle was a sphere-cone with a base diameter of 1.5 m. The freestream velocity and entry angle were 10.7 km/s and 10°, respectively. Peak stagnation heating took place at 58 km while traveling at 9.5 km/s. The results are shown in Figure 2.10.1
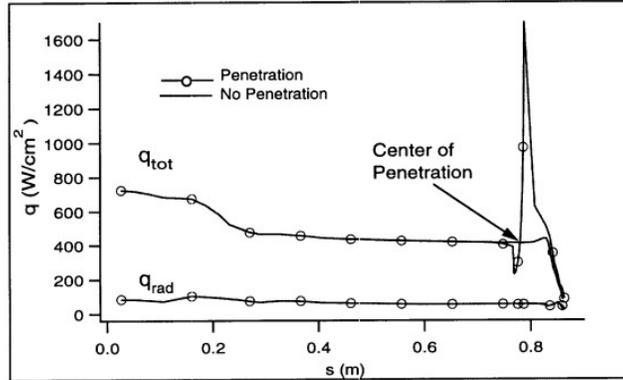
Figure 2.10.1 Heat flux with and without forebody penetration

As results show, the cavity produced by the forebody penetration created a large increase in the heat flux over the area of penetration. The large heat flux increase was likely caused when the flow separated over the front lip of the cavity then reattached at the aft lip where the thinning boundary layer at the back lip raised the heat flux greatly. The original concerns over excessive thermal stresses at the cavity locations causing structural failure were validated. The results were consistent with experimental data from the Apollo Command Module and Genesis missions.

2.11 Blowing of Ablative Gases

Martin and Boyd [13] examined the effects of blowing of pyrolysis gas into the boundary layer and outer flowfield. In charring ablators, the resin underneath the surface goes through pyrolysis at a relatively low temperature and the gases that escape into the boundary layer go through complex chemical reactions with the surrounding gases. Using the Stardust mission as a benchmark, the study utilized data from six different positions of Stardust's entry trajectory for comparisons. The chemistry models used in this study were selected with a material response analysis, which was optimized and developed for PICA heat shields. The kinetic chemistry rates were derived from the GRI-MECH model and optimized with a sensitivity analysis. The chemical species were grouped into three categories:

1. Air Species: N_2, O_2, NO, N, O, N_2^+, O_2^+, NO^+, N^+, O^+, e
2. Surface Species: H_2, CO, CH_4, H_2O, CO_2, OH, C_2H_2, HCN, C_2H, C_3, CN
3. Reacting Species: H, NH, HO_2, H_2O_2, HCO, C, C_2, CH, CH_2, CH_3, NCO, HNO, CO^+, CN^+, C^+, H^+

The equilibrium constants required to solve the backward reaction rates were provided by Gibb's Free Energy. The program CHEMKIN was used to calculate the transport properties of the gases. The aeroheating environment was estimated using the Data Parallel Line Relaxation; the heat transfer coefficient, the surface pressure, and the freestream enthalpy were input into FIAT. The pressure and the non-dimensionalized ablation rate produced by FIAT were then imported to the Multicomponent Ablation Thermochemistry code. With the appropriate input values, MAT was able to calculate the species mole fractions that corresponded to the wall temperatures estimated by FIAT. The above procedure was able to produce the input values of wall temperature, blowing rates, and equilibrium species composition. The equilibrium condition calculations included the surface materials and boundary layer edge gases, and therefore accounted for surface ablation. A linear relationship between the mass flow rate and temperature was derived using wall conditions at the stagnation point captured by the Echelle instrument.

11

According to the results, most of the blowing gas species were destroyed upon entering the flow field. Of the remaining species, CO, OH, CN, and CN$^+$ had relatively high concentrations and were significant due to their intense radiative properties. Atomic species H and C were highly concentrated near the boundary. Further examination showed that a notable effect of blowing gases was the displacement of the shock. Having the shock being further away from the surface of the vehicle directly affected the temperature gradient at the wall. However, it was found that the conductivity of the gases had a significantly greater influence on heat flux. The results showed that the composition of gases in the boundary layer had a greater overall contribution to heat flux reduction than altitude effects and blowing rate. After plotting the heat flux at all six trajectory points, the translational-rotational energy was shown to be the biggest contributing factor. It was observed that the amount of blowing and the translational-rotational heat flux had a direct and linear relationship. Although an increase in blowing rates could have impacted the overall heat flux, it was not a significant contributor of heat flux.

2.12 Stagnation Point Convective Heating Equation

A method for calculating the stagnation point convective heating of a blunt, axisymmetric entry vehicle for gas mixtures in chemical equilibrium during atmospheric entry was provided [14]. Convective thermal behavior of gas particles around an entry vehicle is fully dependent on the composition of gases in the specific atmosphere. It is important to note that with the exception of Earth, the actual chemical compositions of the atmospheres of the other planets are not exactly known. Basic heat transfer theories were used to derive a simple approximation relationship. Calculations for convective heating of various gas compositions were done by an existing computer code. The convective heating calculations were used in developing the approximate general relation. After a lengthy derivation, the authors presented the convective heating at the stagnation point of a blunt, axisymmetric body as

$$\dot{q}_{sc} = \sqrt{\frac{p_s}{r_{eq,b}}} \frac{0.58(8)^{1/4}}{\left(N_{Pr,w}\right)^{0.6}} \left(\frac{M_e}{RT_e}\right)^{1/4} \left(\frac{M_o}{M_e}\right)^{1/8} (\mu_{o,e})^{1/2} (h_s - h_w) \left[1 - \frac{\beta_{2,w}}{M_w (N_{i,w})^{\frac{1}{3}}} \cdot \frac{\sum F_i h_{i,w}(z_{i,e} - z_{i,w})}{h_s - h_w} + (N_{i,w})^{2/3} \sum \right.$$

(2.12.1)

It was shown that the convective heating at the stagnation point for gases is a function of the mass fraction, molecular weight, and transport parameters of the gas mixtures.

2.13 Ballistic Coefficient

An analysis was presented on the accuracy of the methods of estimation for finding the ballistic coefficient of a re-entry vehicle [15]. When an object enters an atmosphere, it is bombarded by a sudden increase in atmospheric density due to the presence of gases. Relative to the near vacuum conditions in outer space, the gases are high in viscosity and act as a barrier to decrease the velocity of anything that wishes to travel through the atmosphere. The ballistic coefficient is a measure of the ability of an object to resist the deceleration as it travels through a medium. An object with a higher ballistic coefficient will be able to travel further, faster, more stable, or a combination of all three. Being able to estimate the ballistic coefficient of an object has a great amount of applications, including the tracking of re-entry vehicles. Many radars, like

the millimeter wave radar, use adapted sensors to locate re-entry vehicles that transition from the calm exo-atmospheric environment to the violent endo-atmospheric environment. The sudden deceleration caused by the aerothermal loads on the object can be observed and used to determine the ballistic coefficient. Knowing the kinematic behaviors and the ballistic coefficient allows the radars to determine the location of the object and predict its trajectory.

The authors chose the Allen re-entry model to help represent the 2D re-entry scenario. The zero-incidence, endo-atmospheric model only considered the drag forces on the vehicle and neglected any lift generated. To apply the Allen model, the following conditions were assumed

1. The ballistic coefficient and flight path angle were constant throughout the scenario
2. The flight path angle is known
3. Restricted to a two-dimensional model
4. The re-entry vehicle was statically and dynamically stable
5. Ablation was minimal and did not generate structural or aerothermal asymmetries
6. Gravity was negligible during the deceleration phase

Using the Fisher Information Matrix and the Monte-Carlo analysis, the authors investigated the accuracy of a closed-form approximation to the Cramer-Rao lower bound method. Using the FIM and range only measurements, a closed-form expression of a lower bound on the discrepancy of a ballistic coefficient estimation was provided. With the expression, a CRB approximation of the estimation of the ballistic coefficient can be derived. It could be shown that the lower bound on the discrepancy of a ballistic coefficient estimation was a function of dynamic pressure. Therefore, a sudden deceleration caused by the atmospheric density was directly related to the accuracy of the estimations.

The authors were able to establish an excellent relationship between the methods of estimation for the ballistic coefficient, as seen in Figure 2.13.1.
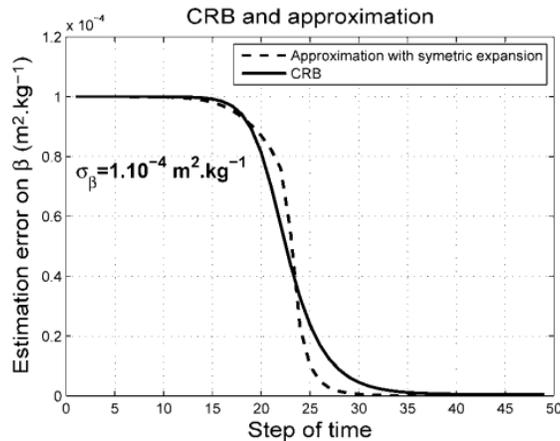
Figure 2.13.1 Ballistic coefficient estimation error bounds

3.0 Project Objective

The purpose of this master's project is to analyze the aerothermodynamics of re-entry vehicles performing aerocapturing and skip re-entry maneuvers. The one-dimensional stagnation point heat flux, recession depth, heat loads, and pyrolysis and ablation quantities experienced during the maneuvers will be produced. The TPS thickness necessary to survive the aerocapture and skip re-entry will also be calculated. Along with various assumptions, the three main inputs required by FIAT for TPS sizing calculations are:

1. Surface Energy Balance Option
    I.   Surface Ablation
    II. Assigned Temperature and Recession Rate
    III. Non-Ablating with Radiation
    IV. Non-Ablating without Radiation
2. Materials used and material configuration of the heat shield
3. Chemical composition of target environment/atmosphere

A parametric study will be conducted where the inputs such as environment and surface temperatures are varied within a range so that the optimal TPS sizing that will ensure protection of the vehicle across multiple scenarios can be found. The aerothermal outputs produced will be compared to the SRC aerothermodynamics of the Stardust mission during its Earth re-entry.

4.0 Methodology

This project aims to combine the results produced by FIAT and Mars SRC and compare them with the aerothermodynamics of the Stardust SRC re-entry for analysis. Permission for the program FIAT must be acquired from NASA Ames Research Center before it can be implemented. To ensure a purposeful analysis, TACOT TPS material is selected for use in FIAT. TACOT is a theoretical material that has been utilized in a few studies as an ablation test benchmark [17, 18]. The pyrolyzing properties of TACOT are very similar to the properties carbon-phenolics such as PICA, the Stardust SRC TPS materials. PICA is unfortunately not an input material offered by FIAT in its exact form. A sample lunar return skipping trajectory scenario has been hardcoded into FIAT and can be readily utilized by users. To accurately reproduce the skipping trajectory environment, the following inputs are provided for each timestep:

1. Recovery enthalpy
2. Radiative and other non-convective heat fluxes
3. Heat transfer coefficient
4. Dynamic pressure
5. Blowing parameter
6. Freestream fluid temperature

Using the sample skip trajectory environment as a baseline, efforts were made to match input values to the skip re-entry trajectory environments proposed in [3, 19]. The initial temperature and bondline interface thermal limits of TACOT and subsequent internal TPS linings were input for TPS sizing calculations. The freestream temperature, dynamic pressure, and non-convective heat fluxes experienced by the vehicle in Earth's atmosphere were set to recreate the skip trajectory environment. The disastrous formatting of FIAT outputs will prevent the graphing of many meaningful aerothermal results; each result has several thousands of values that need to be

manually transferred into a graphing software (e.g. Microsoft Excel) before it can be graphed. Consequently, only the results with a relatively manageable amount of values will be attempted for graphing. Some numerical results can be found in Appendix C and D.

5.0 Results and Discussion

The Stardust SRC return trajectory was typical of an unmanned return capsule; it was observed to have closely followed the predicted flight profile and landed well within the target range. The aerothermodynamic and material response data of the SRC were collected as described in Section 2.3 and were input to the DPLR CFD code for heating estimations. The two sample cores that were extracted (Figure B.1) from the SRC heatshield were further divided into sections and sent to Lockheed Martin Space Systems, NASA JSC, and NASA ARC for analysis. Examination of the core density profiles (Figure B.2) shows clear transitions of the PICA material between char, pyrolysis, and virgin states. Notice that a greater char depth was seen on the flank core than on the stagnation core. This peculiarity can be explained by the higher instantaneous heat flux and thus a higher ablation rate experienced at the stagnation point. The remaining amount of the virgin PICA material was tested for signs of structural degradation from exposures to space and re-entry environments. The test yielded normal strength values that fell within the average range of virgin PICA strength values, suggesting that no structural degradation was experienced in flight [16]. Recession at the stagnation point was determined by taking the difference between the pre- and post-flight TPS thicknesses; a recession of 0.57 cm was measured, the estimated error was the result of instrument limitations and imperfect core extraction techniques.

FIAT simulated the lunar return skipping trajectory using the highest integrated heat load on a vehicle similar to NASA's Crew Exploration Vehicle. The skipping vehicle experienced a high heat pulse during its initial entry into the atmosphere, greatly reducing its velocity. It then lifted out for a cooldown phase before committing to the final entry, where it sustained a second heat pulse of lower magnitude but longer duration. The total simulated flight duration was 1211 s. During the first heat pulse, the pyrolyzing TACOT gas blowing rate was greater than the char ablation rate (Appendix C). During the second heat pulse, with the composite surface phenolic resin depleted, the pyrolysis gas blowing rate was less than the char ablation rate. The upper TPS plies were sized with a temperature constraint of 611 K, slightly below the thermal failure threshold of the experimental TACOT. Besides providing the inputs as discussed in Section 4.0, the typical trajectory parameters were not required by FIAT (e.g. entry velocity, flight path angle, vehicle geometry) to produce the lunar return skip re-entry.

The stagnation heat flux and heat load of the Stardust SRC were 1000 W/cm^2 and 27.2 kJ/cm^2, respectively. It can be seen that the peak heat flux occurred roughly 50 s after atmospheric entry (Figure B.3), where the sudden interaction with the atmosphere greatly decreased the vehicle velocity, resulting in large thermal energy dissipation. Those values were expectedly higher than that of the aerocapturing Mars SRC. The Stardust SRC entered at a higher velocity, a steeper flight path angle, and traveled through the atmosphere for a longer duration (Figure B.4). The Mars SRC had a high convective heat flux which peaked around 80 s after atmospheric interaction (Figure B.5) but a relatively low radiative heat flux (Figure B.6) due to its small effective radius. The Mars SRC lifted back out of the atmosphere at an altitude of 68.9 km (Figure B.7) while the Stardust SRC continued through the denser lower atmosphere for its eventual landing. As a result of the greater stagnation point heat flux experienced by the Stardust

SRC, a thicker initial PICA TPS was required. However, the nominal thickness and the scant amount in recession of the AVCO-5026 was in part due to its greater material density. The AVCO-5026, being nearly twice as dense as the PICA, was more capable of withstanding extreme thermal interactions. A benefit of aerocapturing a vehicle over employing a strictly propulsive maneuver is the reduction in fuel mass penalties. The Mars SRC was able to make use of a denser heatshield with a lower rate of ablation which consequentially increases its reusability.

The aerothermodynamics of the skip re-entry vehicle was unexpectedly higher than that of the direct entry Stardust SRC. The radiative and total stagnation heat flux, peak surface temperature, and stagnation heat load were 730.7 W/cm^2, 1301.3 W/cm^2, 3283 K, and 27.7 kJ/cm^2, respectively. The peak of the first heat pulse occurs 74 s into the flight and the second heat pulse with a surface temperature of 2253.9 K peaks at 545 s (Figure B.8). The values are summarized in Table 5.1. There are several possible explanations for this abnormal behavior. In simulating the skip re-entry trajectory, FIAT did not allow users to directly input entry velocity, flight path angle, or vehicle geometry, all of which play a significant role in re-entry aerothermodynamics. The input format provided by FIAT is solely based on the trajectory environment of the vehicle. Although a sample skip re-entry trajectory was provided in the program as a baseline, it would be extremely difficult for users to recreate the desired vehicle trajectory environment without the help of an external trajectory simulator.

The combined aerothermal results of the aerocapture and skip re-entry maneuvers proved to be unfavorable compared to the direct entry maneuver. The direct entry maneuver experienced lower combined heat flux, surface temperatures, heat loads, TPS recession, shorter flight duration, and required less TPS material for protection. However, the results are reinforced by the fact that no American spacecraft has ever executed a real skip re-entry; the Apollo and Space Shuttle missions utilized some lifting maneuvers but never actually left the atmosphere.

Table 5.1 Aerothermodynamics comparison of return capsules

	STARDUST SRC	AEROCAPTURE	SKIP RE-ENTRY
Forebody TPS	PICA	AVCO-5026	TACOT
VIRGIN MATERIAL DENSITY (KG/M^3)	270	513	274
Entry velocity (km/s)	12.8	11.8	-
ENTRY ANGLE (DEG)	-8.2	-5.7	-
Flight Duration (s)	780	425	1211
PEAK STAGNATION POINT TOTAL HEAT FLUX (W/CM^2)	1000	260.7	1301.3
PEAK STAGNATION POINT RADIATIVE HEAT FLUX (W/CM^2)	84	36.9	730.7

Peak Surface Temperature (K)	3000	2900	3283
PEAK STAGNATION POINT HEAT LOAD (KJ/CM²)	27.2	14.8	27.7
Initial TPS Thickness (cm)	5.82	1.26	8.28
Stagnation Point Recession (cm)	0.57±0.03	0.04	2.61

6.0 Conclusion and Future Work

The aerothermodynamic results of the Stardust SRC demonstrated the promising capabilities of the PICA TPS. It enabled the SRC to re-enter the atmosphere at speeds faster than any other man-made object and suffered nominal ablative losses. The low-density property of the PICA extends the range and capabilities of future re-entry vehicles. The aerocapturing maneuver proved to be an excellent method for reducing fuel mass penalties. The relatively mild aerothermal loads of aerocapturing allow spacecrafts to reduce the required amount of TPS material and fuel for retro-propulsion, which ultimately reduce costs and increase mission efficiency. The skip re-entry maneuver performed similarly to the direct entry in most categories. The longer flight duration, along with an imprecise method of skip trajectory simulation could have contributed to the higher than expected final results. It is assumed that a high-fidelity skip trajectory simulation that models an SRC re-entry scenario comparable to the first two maneuvers will produce more desirable results. As the demand for more efficient methods of space travel increases, maneuvers that decrease fuel and overall costs, such as aerocapturing and skip re-entry, will increase in popularity.

There are numerous trajectory simulators capable of producing a skip trajectory. One particular program with tremendous heritage is POST, which was originally designed for Space Shuttle trajectory optimizations. The outputs from a properly designed skip trajectory, which is a project in and of itself, can be used as environment inputs in FIAT. An integrated program that combines a trajectory simulator, chemical thermal response of materials, and TPS sizing will greatly improve the transfer of data between programs and be self-sufficient.

References

[1] Williams, S. D., Gietzel, M. M., Rochelle, W. C., and Curry, D. M., "TPS Design for Aerobraking at Earth and Mars," *NASA Technical Memorandum 104739*, August 1991, Lyndon B. Johnson Space Center, Houston, Texas.
https://ntrs.nasa.gov/archive/nasa/casi.ntrs.nasa.gov/19910021656.pdf

[2] Carpenter, R., "Current Systems Analysis: Aeroassist Flight Experiment," *Texas Space Grant Consortium*, 2 November 1992.
http://www.tsgc.utexas.edu/archive/PDF/AeroassistFlightExp.pdf

[3] Brunner, C. W., "Skip Entry Trajectory Planning and Guidance," *Retrospective Thesis and Dissertations*, 2008, Iowa State University, Ames, Iowa.
http://lib.dr.iastate.edu/cgi/viewcontent.cgi?article=16811&context=rtd

[4] Kontinos, D. A. and Stackpoole, M., "Post-Flight Analysis of the Stardust Sample Return Capsule Earth Entry," *46th AIAA Aerospace Sciences Meeting and Exhibit*, 7-10 January 2008, Reno, Nevada.
http://highorder.berkeley.edu/proceedings/aiaa-annual-2008/paper0899.pdf

[5] Covington, M. A., "Performance of a Light-Weight Ablative Thermal Protection Material For the Stardust Mission Sample Return Capsule," ELORET Corp., Sunnyvale, California.
https://ntrs.nasa.gov/archive/nasa/casi.ntrs.nasa.gov/20070014634.pdf

[6] Weng, H. and Martin, A., "Numerical Investigation on Charring Ablator Geometric Effects: Study of Stardust Sample Return Capsule Heat Shield," *53rd AIAA Aerospace Science Meeting and Exhibit*, 5-9 January 2015, Kissimmee, Florida. DOI: 10.2514/6.2015-0211
http://uknowledge.uky.edu/cgi/viewcontent.cgi?article=1024&context=me_facpub

[7] Milos, F. S. and Chen, Y. -K., "Ablation and Thermal Response Property Model Validation for Phenolic Impregnated Carbon Ablator," *47th AIAA Aerospace Science Meeting and Exhibit*, 5-8 January 2009, Orlando, Florida.
https://ntrs.nasa.gov/archive/nasa/casi.ntrs.nasa.gov/20110012891.pdf

[8] Dec, J. A., Braun, R. D., "An Approximate Ablative Thermal Protection System Sizing Tool for Entry System Design," *44th AIAA Aerospace Sciences Meeting and Exhibit*, 9-12 January 2006.
http://soliton.ae.gatech.edu/labs/ssdl/papers/conferencePapers/AIAA-2006-0780.pdf

[9] Milos, F. S., Chen, Y. -K., and Squire, T. H., "Updated Ablation and Thermal Response Program for Spacecraft Heatshield Analysis," *17th Thermal and Fluids Analysis Workshop*, 11 Aug. 2006.
https://tfaws.nasa.gov/TFAWS06/Proceedings/Aerothermal-Propulsion/Papers/TFAWS06-1008_Paper_Squire.pdf

[10] Rindal, R. A., "An Approach for Characterizing Charring Ablator Response with In-Depth Coking Reactions," *NASA CR-1065*, June 1968.
https://ntrs.nasa.gov/archive/nasa/casi.ntrs.nasa.gov/19680017345.pdf

[11] Viviani, A. and Pezzella, G., "Nonequilibrium Aerothermodynamics for a Capsule Reentry Vehicle," *Engineering Applications for Computational Fluid Mechanics*, Vol. 3, No. 4, pp. 543-561. DOI: 10.1080/19942060.2009.11015290
http://dx.doi.org/10.1080/19942060.2009.11015290

[12] Olynick, D. and Kontinos, D., "Aerothermal Effects of Cavities and Protuberances for High-Speed Sample Return Capsule," NASA Ames Research Center, Moffett Field, California.
https://ntrs.nasa.gov/archive/nasa/casi.ntrs.nasa.gov/20020061283.pdf

[13] Martin, A. and Boyd, I.D., "Modeling of heat transfer attenuation by ablative gases during the Stardust re-entry," *50th AIAA Aerospace Sciences Meeting and Exhibit*, 9-12 January 2012, Nashville, Tennessee. DOI: 10.2514/6.2012-814
http://uknowledge.uky.edu/cgi/viewcontent.cgi?article=1011&context=me_facpub

[14] Sutton, K, and Graves, R. A., "A General Stagnation-Point Convective-Heating Equation for Arbitrary Gas Mixtures", *NASA TR R-376*, 1971.
https://ntrs.nasa.gov/archive/nasa/casi.ntrs.nasa.gov/19720003329.pdf

[15] Dodin, P., Minvielle, P., and Le Cadre, J. P., "Estimating the Ballistic Coefficient of a Re-Entry Vehicle," *Institute of Engineering and Technology Radar Sonar Navigation*, Vol. 1, No. 3, 2007, pp. 173-183.
http://www.irisa.fr/vista/Papers/2007_rsn_dodin.pdf

[16] Stackpoole, M., Sepka, S., Cozmuta, I., and Kontinos, D., "Post-Flight Evaluation of Stardust Sample Return Capsule Forebody Heatshield Material," *46th AIAA Aerospace Sciences Meeting and Exhibit*, 7-10 January 2008, Reno, Nevada.
http://highorder.berkeley.edu/proceedings/aiaa-annual-2008/paper0900.pdf

[17] Lachaud, J., Martin, A., Eekelen, T., and Cozmuta, I., "Ablation Test-Case Series #2," *Numerical Simulation of Ablative-Material Response*, 1 September 2011.
http://ablation2012.engineering.uky.edu/files/2012/02/Test_Case_2.pdf

[18] Alkandry, H., Boyd, I. D., and Martin, A., "Coupled Flow Field Simulations of Charring Ablators with Nonequilibrium Surface Chemistry," *44th AIAA Thermophysics Conference*, 24-27 June 2013, San Diego, California.
https://pdfs.semanticscholar.org/58cb/c8d8dec76e0eb369941a80df7c493eec5776.pdf

[19] Rea, J. R. and Putman, Z. R., "A Comparison of Two Skip Entry Guidance Algorithms," *AIAA Guidance, Navigation, and Control Conference*, 20-23 August 2007, Hilton Head, South Carolina.
https://ntrs.nasa.gov/archive/nasa/casi.ntrs.nasa.gov/20070023643.pdf

Appendix A: Derivation of Governing Equations

The derivation of the governing equations for the program FIATv3 will be shown below.

FIATv3:

The decomposition of solids is modeled using three components, A, B, and C, where A and B are the resin, and C is the reinforcing material. The composite density is calculated using

$$\rho = (1-\phi)[\Gamma(\rho_A + \rho_B) + (1-\Gamma)\rho_C] \tag{A.1}$$

Each component (i = A, B, C) of the solid decomposes independently and can be modeled using the Arrhenius-type reaction

$$\frac{d\rho_i}{dt} = -A_i \rho_{iv} \left(\frac{\rho_i - \rho_{ic}}{\rho_{iv}}\right)^{\psi_i} \exp\left(\frac{-E}{RT}\right) \tag{A.2}$$

Virgin density
$$\rho_v = (1-\phi)[\Gamma(\rho_{Av} + \rho_{Bv}) + (1-\Gamma)\rho_{Cv}] \tag{A.3}$$

Char density
$$\rho_c = (1-\phi)[\Gamma(\rho_{Ac} + \rho_{Bc}) + (1-\Gamma)\rho_{Cc}] \tag{A.4}$$

The swelling and shrinkage of the char can be modeled with a relative volume parameter, Φ.

$$\rho' = \rho/\Phi \quad \text{and} \quad V' = V\Phi \tag{A.5}$$

$$\Phi = \Phi_c + (1-\Phi_c)\sum w_i z_i \quad \text{where} \quad \sum w_i = 1 \tag{A.6}$$

Φ_c is a user input and represents the ratio of char-to-virgin volume.

The char and virgin material properties are input with tables provided within FIAT v3. Partially-charred material properties are interpolated using

$$c_p = x c_{p_v} + (1-x) c_{p_c} \qquad x = \frac{\rho_v(\rho - \rho_c)}{\rho(\rho_v - \rho_c)} \tag{A.7}$$

x is the mass fraction of the virgin material in the partially-pyrolyzed zone. The chemical composition of the pyrolysis gas, typically frozen at low temperatures and in equilibrium at high temperatures, must be determined before the enthalpy of the pyrolysis gas can be input into the program.

The front-face boundary conditions are determined using the surface energy balance (SEB). There are four options of boundary conditions to choose from for each execution of the FIAT v3 program. The first option is surface ablation, where diffusion coefficients are assumed to be equal, $C_M = C_H$.
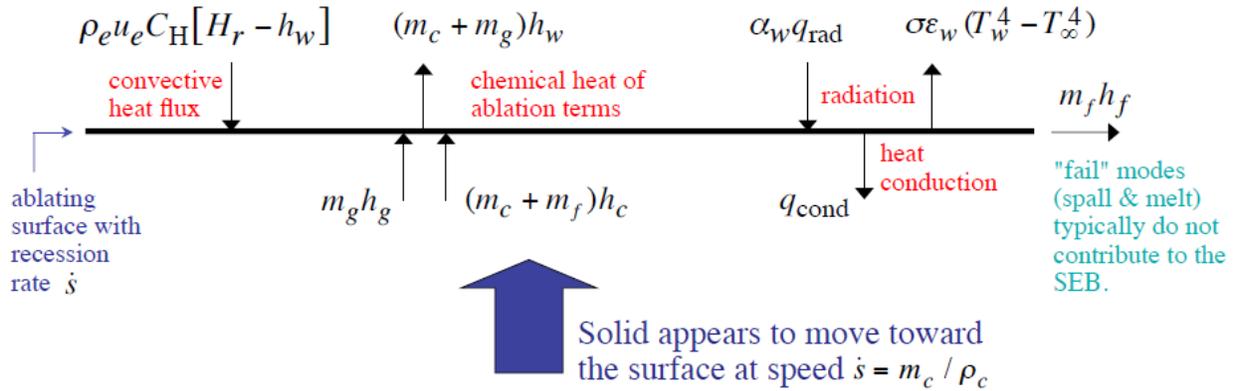
Figure A.1 Surface Energy Balance chart

$$\rho_e u_e C_H \left[H_r - h_w\right] + m_c h_c + m_g h_g + \alpha_w \acute{q}_{rad} - \rho \acute{s}_f \Delta h_f = \left(m_c + m_g\right) h_w + \sigma \varepsilon_w \left(T_w^4 - T_\infty^4\right) + q_{cond}$$

(A.8)

Equation A.8 can be rearranged as

$$\rho_e u_e C_H \left[H_r - \left(1 + B_c' + B_g'\right) h_w\right] + m_c h_c + m_g h_g + \alpha_w \acute{q}_{rad} = \sigma \varepsilon_w \left(T_w^4 - T_\infty^4\right) + \acute{q}_{cond}$$ (A.9)

where $B' = \dfrac{m}{\rho_e u_e C_M}$ is the dimensionless surface mass flow rate, h_g, h_c, H_r, $\acute{q}_{rad}$, $\rho_e u_e C_H$, and T_∞ are input quantities, C_H is the corrected unblown heat transfer coefficient, and m_g, $\acute{q}_{cond}$, and T_w are solution variables. h_w, m_c, and B_c' are calculated using either B' tables.

CFD programs can usually produce an unblown heat flux which allows the unblown hot-wall and cold-wall heat transfer coefficients to be calculated.

$$q_{cfd} = \rho_e u_e C_H \left(H_r - h_w\right) \rightarrow \rho_e u_e C_H = q_{cfd} / \left(H_r - h_w\right)$$

(A.10)

FIAT v3 requires the corrected blown hot-wall value C_H

21

$$C_H = (C_{H1})_{cw} \Omega_{cwhw} \Omega_{blow} = (C_{H1})_{hw} \Omega_{blow} \qquad (A.11)$$

where $\Omega_{cwhw} = \left(\dfrac{\rho_{hw} \mu_{hw}}{\rho_{cw} \mu_{cw}} \right)^{0.2} \approx 1$ is usually ignored, but $\Omega_{blow} = \dfrac{2\lambda B_1'}{\exp\left(2\lambda B_1'\right) - 1} \leq 1$ is

important, λ is an input value that represents the blowing-reduction parameter.

To generate the B' tables, the elemental composition of the atmosphere, pyrolysis gas, and surface char, and the thermodynamic data for selected gas and condensed phase species are required. At each time step in the solution, FIAT reads $\rho_e u_e C_H$, H_r, and P from the input, while B_g' is obtained from m_g. To make the SEB converge, FIAT interpolates B_g' and P to iteratively find the values of B_c'. The B' tables provide the wall-gas enthalpy and ablation rate as functions of wall temperature, pressure, and pyrolysis gas blowing rate.

For a non-ablating material, the SEB becomes

$$\rho_e u_e C_H \left[H_r - h_w \right] = \sigma \varepsilon_w \left(T_w^4 - T_\infty^4 \right) + q_{cond} - \alpha_w q_{rad} \qquad (A.12)$$

The second option of boundary conditions has the recession rate and temperature assigned by the user. The third option is of a non-ablating scenario with radiation, where

$$q_{cond} = q_s + C_T \left(T_F - T \right) + \alpha_w q_{rad} + \sigma \varepsilon_w \left(T_\infty^4 - T^4 \right) - \rho \dot{s}_f' \Delta h_f \qquad (A.13)$$

and the fourth option is of a non-ablating scenario without radiation, where

$$q_{cond} = q_s + C_T \left(T_F - T \right) - \rho \dot{s}_f' \Delta h_f \qquad (A.14)$$

pyrolysis occurs in all four options.

Appendix B: Figures
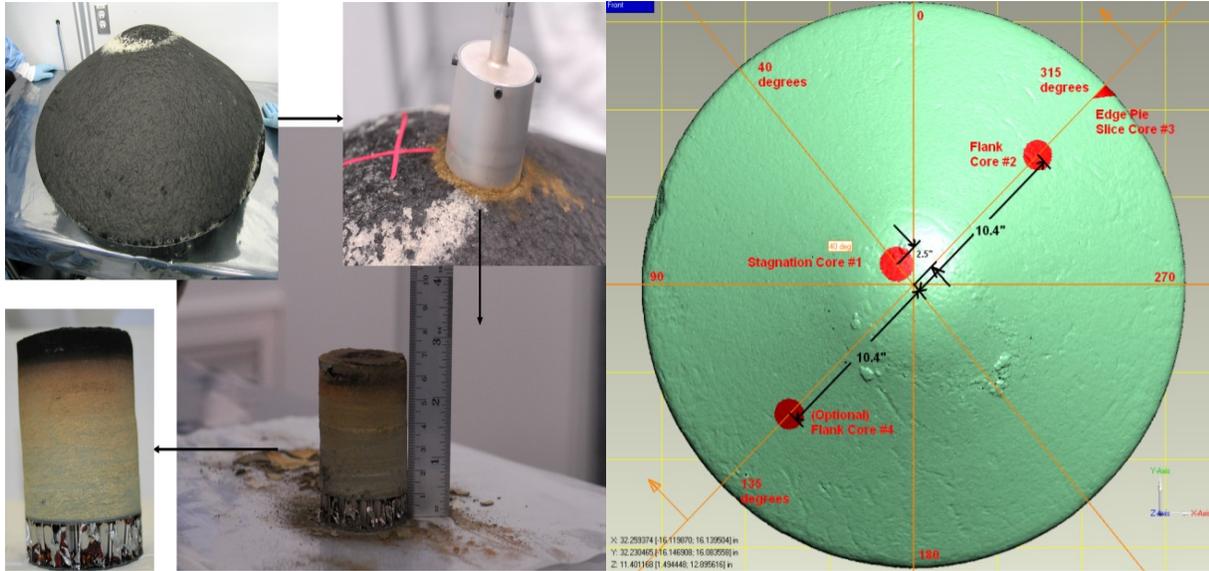
Figure B.1 SRC heatshield core samples
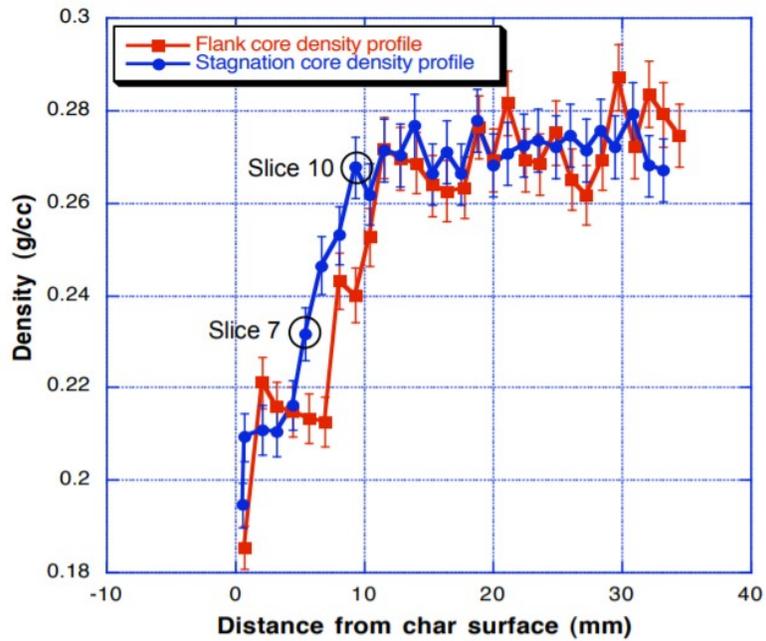
Figure B.2 Core samples density (Slices 1 through 30 correspond with charred surface through bottom of virgin material)
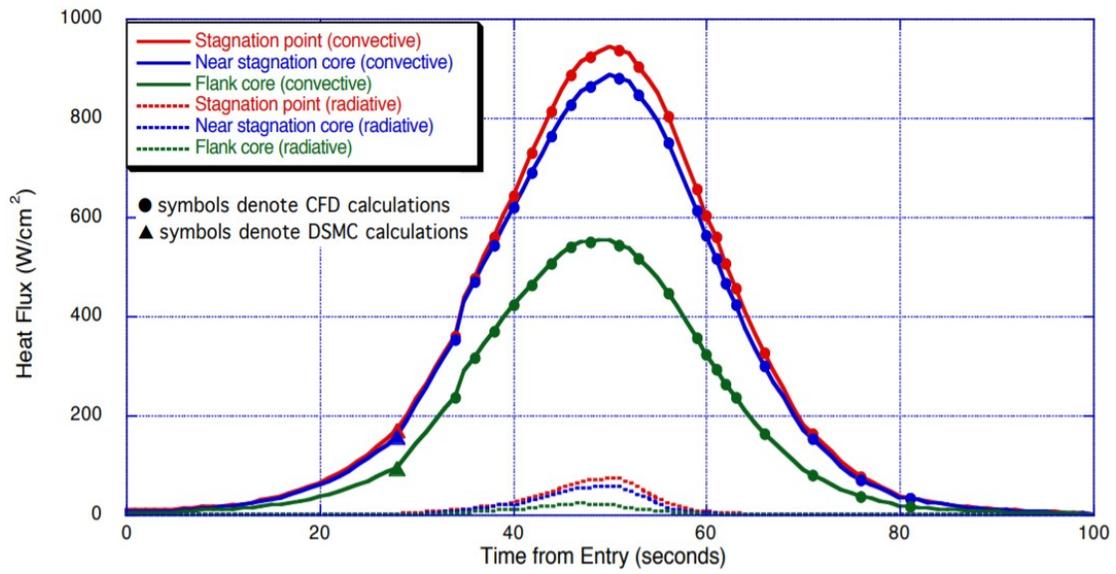
Figure B.3 Stardust SRC heat fluxes
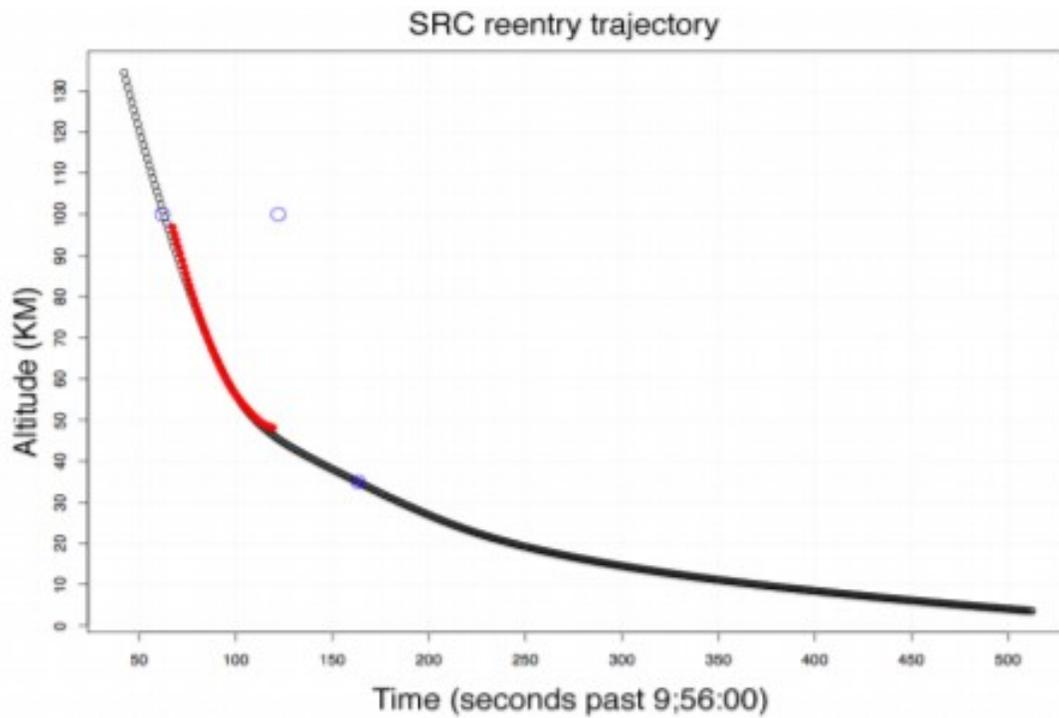
Figure B.4 Stardust SRC trajectory
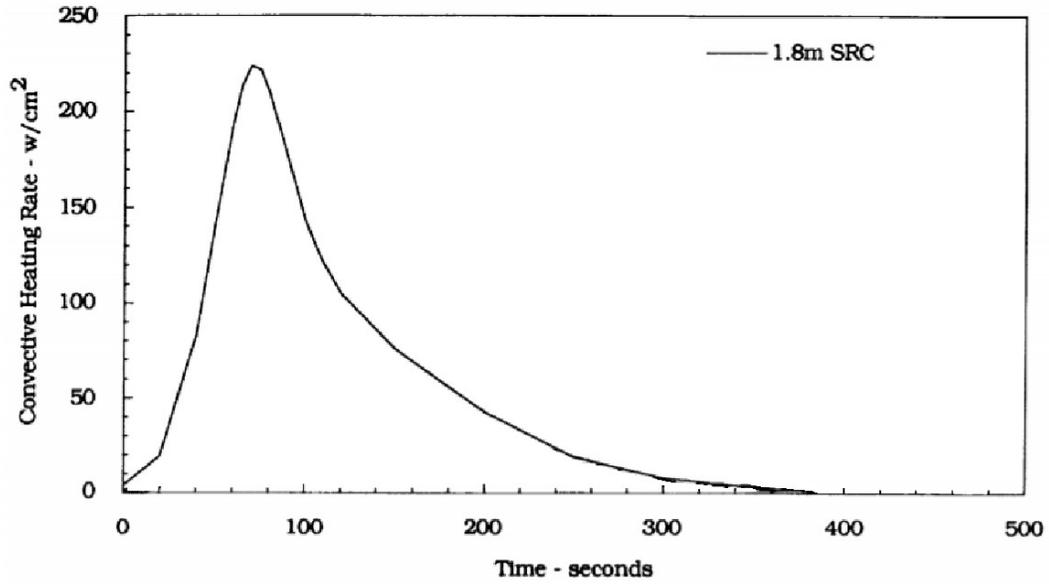
Figure B.5 Mars SRC convective heat flux
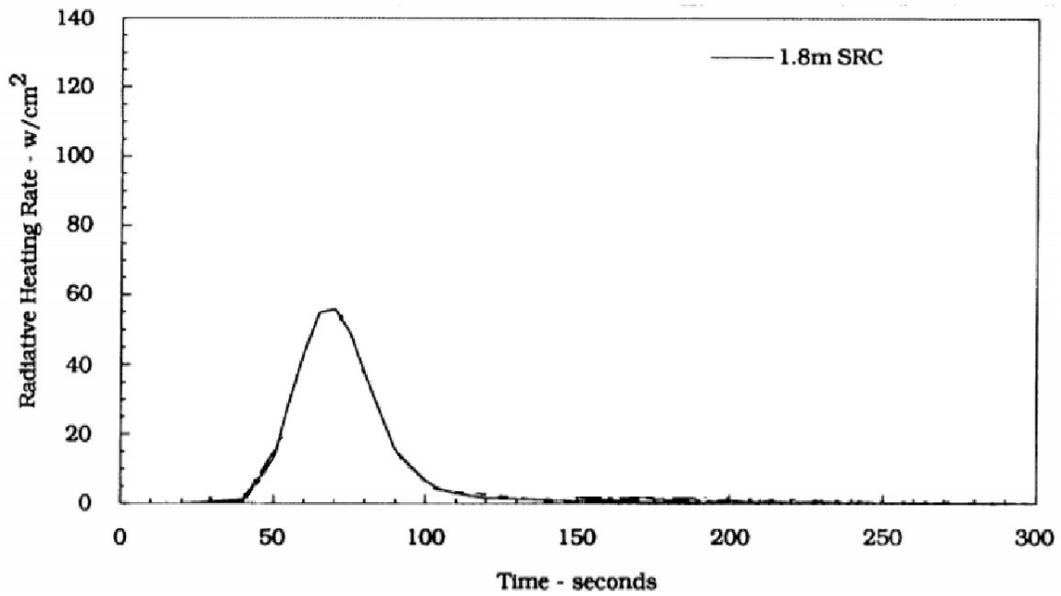
Figure B.6 Mars SRC radiative heat flux

25
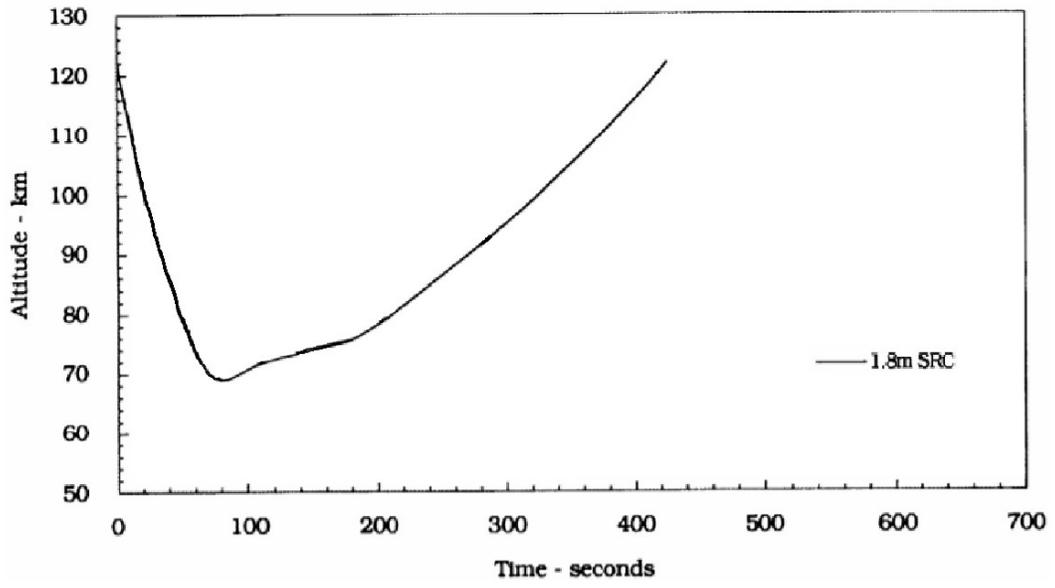
Figure B.7 Mars SRC trajectory
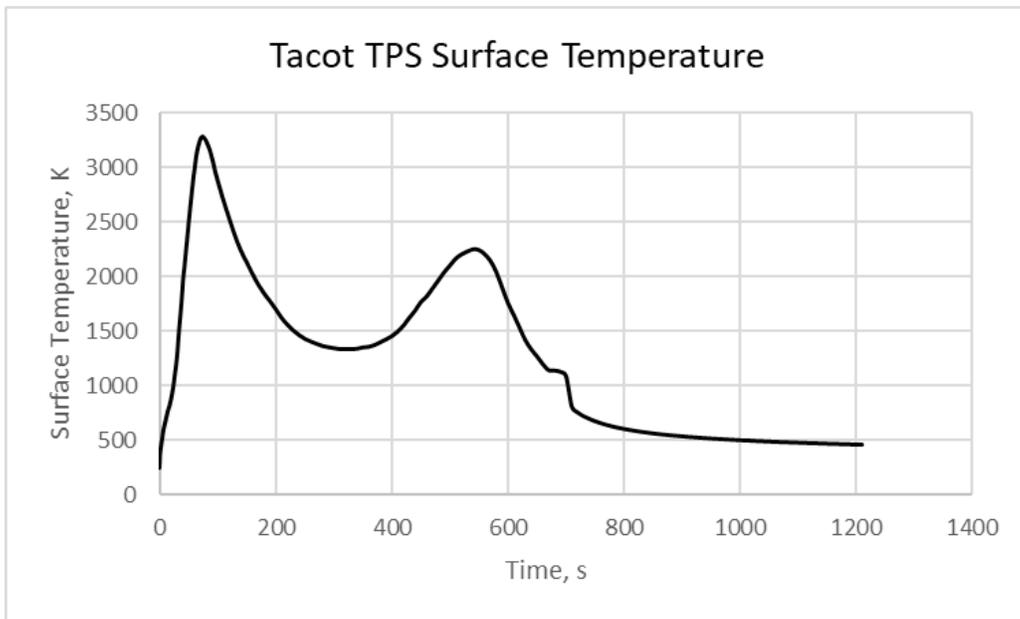
Figure B.8 TACOT surface temperature timeline

Appendix C: FIAT Results at the Two Heat Pulses – 74 s and 545 s

```
- - - - - - - - - - - - - - - FIAT output     74.00000 seconds - - - -
- - - - - - - - - -
NSTP        time     pressure       H edge       H wall       ruch1
lambda    ch/ch1     radtmp        reshtc        rest        shear
           s          Pa           J/kg         J/kg        kg/m2-s
K      W/m2-K         K            Pa
 323    74.00000    20997.58    52345118.    6341752.     0.11645
0.400     0.869     252.778        0.          0.00    0.000E+00


Some surface ablation and pyrolysis quantities (mdot-f includes mass
loss from any global fail model)
     bprime-c    bprime-g    bprime-f       mdot-c       mdot-g
mdot-f  mdot-total  sdot-total    recession    char(2%)  virgin(98%)
                                            kg/m2-s      kg/m2-s
kg/m2-s      kg/m2-s         m/s            m     depth-m     depth-m
  2.7523E-01     0.12069     0.00000   2.784E-02   1.221E-02
0.000E+00   4.005E-02   1.266E-04    0.001748    0.007059    0.012143


Multilayer Pyrolysis   drho term    Ply 01     Ply 02     Ply 03
  mdotg*area, kg/s =    2.439E-05 1.021E-02 1.894E-03 0.000E+00
  Bpg fraction    =       0.00201   0.84176   0.15622   0.00000


Surface energy balance terms and integrated values (option 3 and 4
"other heat flux" is included in "conv in")
         conv in      rad in      rad out    chem gen   conduction
error   fractional      option   iterations     total       spect
          w/m2         w/m2         w/m2         w/m2         w/m2
w/m2       error                              emiss      absorp
rate   5.292E+06    1.658E+06    5.928E+06  -4.431E+05    5.780E+05
4.804E+02   8.104E-05           1          5      0.900       0.900
total  1.099E+08    3.302E+07    1.191E+08  -4.627E+06    1.920E+07 <--
multiply units by s


pt ply  material        node depth      node       temp      density
cp          k    interface   aratio      q cond      m dot g    shrink
s-depth
 #   #  name                     m    aratio      deg k       kg/m3
j/kg-k     w/m-k    depth (m)                   w/m2        kg/m2-s
m

  1  1 TACOT_equil_CEA  0.00174779  0.9930    3283.59     220.188
2149.9      2.243  0.00174779  0.9930    578059.19   1.2184E-02
1.0000  0.00174779
  2  1 TACOT_equil_CEA  0.00188469  0.9925    3248.81     220.194
2148.9      2.189  0.00181624  0.9928    562988.88   1.2187E-02
1.0000  0.00188469
```

```
 10  1 TACOT_equil_CEA  0.00352831 0.9860    2829.80    220.280
2136.1     1.540  0.00338162 0.9866    413927.00  1.2249E-02
1.0000  0.00352831
 20  1 TACOT_equil_CEA  0.00843674 0.9664    1383.02    223.389
1962.8     0.559  0.00805641 0.9680    160310.80  1.2015E-02
1.0000  0.00843674
 30  2 TACOT_equil_CEA  0.01370625 0.9455     681.74    276.336
1593.2     0.473  0.01358171 0.9460     33543.57  8.9212E-04
1.0000  0.01370625
 40  2 TACOT_equil_CEA  0.01772152 0.9295     471.27    279.976
1338.3     0.425  0.01741875 0.9307     16877.34  4.8799E-06
1.0000  0.01772152
 50  3 TACOT_equil_CEA  0.02614036 0.8960     305.04    279.991
999.0      0.403  0.02576116 0.8976      3832.53  0.0000E+00
1.0000  0.02614036
 60  3 TACOT_equil_CEA  0.03591585 0.8572     261.82    279.991
894.7      0.398  0.03529841 0.8596       763.86  0.0000E+00
1.0000  0.03591585
 70  3 TACOT_equil_CEA  0.05183282 0.7939     253.08    279.991
879.2      0.398  0.05082748 0.7979        35.58  0.0000E+00
1.0000  0.05183282
 80  3 TACOT_equil_CEA  0.07774968 0.6908     252.78    279.991
879.2      0.398  0.07611273 0.6973         0.05  0.0000E+00
1.0000  0.07774968
 90  6 RTV-560         0.08545299 0.6602     252.78   1409.584
1096.1     0.423  0.08541489 0.6603         0.00  0.0000E+00
1.0000  0.08545299
 97  7 Ti-6Al-4V       0.08738657 0.6525     252.78   4428.977
552.7      6.744  0.08714844 0.6534         0.00  0.0000E+00
1.0000  0.08738657
 98  7 [back face]                                      252.78
0.08762469 0.6515       -0.00   0.0000E+00            0.08762469
```

**- - - - - - - - - - - - - - FIAT output   545.00000 seconds - - - -
- - - - - - - - - - - (By 545 s, 1st tile has ablated, calculations start
at 2nd tile, pt 25)**

```
NSTP       time    pressure     H edge      H wall      ruch1
lambda   ch/ch1     radtmp      reshtc       rest       shear
           s         Pa         J/kg        J/kg       kg/m2-s
K     W/m2-K         K           Pa
 891  545.00000   16798.67   15222274.   1107869.     0.10326
0.400     0.926    252.778        0.         0.00   0.000E+00
```

Some surface ablation and pyrolysis quantities (mdot-f includes mass
loss from any global fail model)

```
    bprime-c   bprime-g    bprime-f      mdot-c      mdot-g
mdot-f  mdot-total  sdot-total    recession   char(2%) virgin(98%)
                                            kg/m2-s     kg/m2-s
kg/m2-s     kg/m2-s         m/s          m   depth-m    depth-m
```

```
   1.7050E-01     0.03359     0.00000   1.631E-02   3.213E-03
0.000E+00   1.952E-02   7.413E-05   0.013654   0.023663   0.024830


Multilayer Pyrolysis   drho term    Ply 01    Ply 02    Ply 03
  mdotg*area, kg/s =   1.199E-05             1.154E-04 2.911E-03
  Bpg fraction     =      0.00395              0.03797   0.95808


Surface energy balance terms and integrated values (option 3 and 4
"other heat flux" is included in "conv in")
         conv in      rad in     rad out    chem gen  conduction
error  fractional       option  iterations    total      spect
         w/m2         w/m2       w/m2         w/m2         w/m2
w/m2       error                            emiss    absorp
rate   1.455E+06   0.000E+00   1.316E+06  -4.967E+04   8.944E+04
6.889E+01   4.734E-05          1         5     0.900     0.900
total  5.464E+08   5.096E+07   5.298E+08  -1.580E+07   5.178E+07 <--
multiply units by s



pt ply  material          node depth     node       temp     density
cp        k   interface  aratio      q cond     m dot g    shrink
s-depth
 #   #  name                     m   aratio     deg k      kg/m3
j/kg-k     w/m-k   depth (m)                   w/m2      kg/m2-s
m

 25  2 TACOT_equil_CEA 0.01365418  0.9457    2253.92     220.165
2111.2      0.953  0.01365418  0.9457     89440.64   3.2003E-03
1.0000  0.01365418
 30  2 TACOT_equil_CEA 0.01458483  0.9420    2166.21     220.190
2106.3      0.884  0.01446965  0.9425     85025.99   3.2100E-03
1.0000  0.01458483
 40  2 TACOT_equil_CEA 0.01829842  0.9272    1801.74     220.354
2071.2      0.666  0.01801840  0.9283     67747.10   3.2485E-03
1.0000  0.01829842
 50  3 TACOT_equil_CEA 0.02614036  0.8960    1175.15     222.412
1871.6      0.532  0.02576116  0.8976     31182.81   3.2277E-03
1.0000  0.02614036
 60  3 TACOT_equil_CEA 0.03591585  0.8572     804.07     252.010
1670.8      0.483  0.03529841  0.8596     12242.38   1.5854E-03
1.0000  0.03591585
 70  3 TACOT_equil_CEA 0.05183282  0.7939     562.53     276.465
1466.8      0.454  0.05082748  0.7979      5754.07   2.6886E-04
1.0000  0.05183282
 80  3 TACOT_equil_CEA 0.07774968  0.6908     351.47     279.991
1098.5      0.408  0.07611273  0.6973      1808.24   4.4688E-08
1.0000  0.07774968
 90  6 RTV-560         0.08545299  0.6602     278.18    1409.584
1119.4      0.415  0.08541489  0.6603       932.76   0.0000E+00
1.0000  0.08545299
```

```
 97  7 Ti-6Al-4V          0.08738657  0.6525     277.50    4428.977
552.7      7.050  0.08714844  0.6534       212.30   0.0000E+00
1.0000  0.08738657
 98  7 [back face]                               277.50
0.08762469  0.6515            0.00   0.0000E+00            0.08762469
```

Appendix D: FIAT Ablation Data

```
FIAT version 3.1.2 January 2017 NASA Ames
Title: Same as DAC2-TACOT-3tile
Environment: DAC2 environment with high heat load
     convection scaling factor HFACT =  1.000  multiplies CT and CH in
SEB options 1, 3, and 4
     radiation  scaling factor RFACT =  1.000  multiplies Qrad in SEB
options 1 and 3
     recession  scaling factor SFACT =  1.000  adds (this factor -
1)*(bpf+bpc) to bpf
     failure    scaling factor FFACT =  0.000  adds (this factor)*bpc
to bpf
     other      scaling factor OFACT =  1.000  multiplies Qs in SEB
options 3 and 4
Using a case-specific material deck  (not the FIAT Material Database
File)
     Matl.  1 = TACOT_equil_CEA                  thick= 0.01270 meters
TTT angle =  0.000 degrees
     Matl.  2 = TACOT_equil_CEA                  thick= 0.01270 meters
TTT angle =  0.001 degrees
     Matl.  3 = TACOT_equil_CEA                  thick= 0.05742 meters
TTT angle =  0.000 degrees
     Matl.  4 = RTV-560                          thick= 0.00030 meters
     Matl.  5 = SIP                              thick= 0.00229 meters
     Matl.  6 = RTV-560                          thick= 0.00030 meters
     Matl.  7 = Ti-6Al-4V                        thick= 0.00190 meters
Thickness optimization of material  3 based on max temp at bottom of
material  3 =  1009.67
Geometry type is: EXTERNAL CYLINDRICAL
Convergence criteria are: TIGHT
Atmosphere type: Earth
Species File: From CEA database + Burcat C3H & C4H, 128 gas species
with elements HHeCNOSiAr


Unit 27: Pyrolysis and ablation quantities vs time.
         Depths measured from initial surface.


pyrolysis zone range
     time       Tw       mdotg       mdotc       mdotf  mdottotal
recession   char(2%)   virgin(98%)
     sec        K      kg/m2-s     kg/m2-s     kg/m2-s    kg/m2-s
m          m           m


    0.000   252.78  0.000E+00   0.000E+00   0.000E+00   0.000E+00
0.000000    0.000000    0.000000
    1.000   381.59  1.305E-05   4.782E-05   0.000E+00   6.087E-05
0.000000    0.000000    0.000000
    2.000   429.30  1.348E-05   4.871E-05   0.000E+00   6.218E-05
0.000000    0.000000    0.000000
```

```
    3.000    469.17  1.567E-05  5.311E-05  0.000E+00  6.878E-05
0.000001   0.000001   0.000001
    4.000    503.39  2.000E-05  5.640E-05  0.000E+00  7.640E-05
0.000001   0.000001   0.000001
    5.000    537.76  3.184E-05  6.233E-05  0.000E+00  9.417E-05
0.000001   0.000001   0.000001
    6.000    573.61  6.047E-05  6.528E-05  0.000E+00  1.258E-04
0.000001   0.000001   0.000001
    7.000    604.17  1.153E-04  6.238E-05  0.000E+00  1.777E-04
0.000002   0.000002   0.000002
    8.000    630.15  2.031E-04  5.312E-05  0.000E+00  2.562E-04
0.000002   0.000002   0.000002
    9.000    655.75  3.430E-04  4.249E-05  0.000E+00  3.855E-04
0.000002   0.000002   0.000045
   10.000    675.35  5.075E-04  1.829E-05  0.000E+00  5.258E-04
0.000002   0.000002   0.000302
   50.000   2483.83  1.195E-02  4.336E-03  0.000E+00  1.629E-02
0.000088   0.002253   0.009426
   70.000   3252.96  1.231E-02  2.432E-02  0.000E+00  3.663E-02
0.001270   0.006250   0.012119
   71.000   3265.52  1.232E-02  2.544E-02  0.000E+00  3.776E-02
0.001383   0.006431   0.012125
   72.000   3275.50  1.231E-02  2.649E-02  0.000E+00  3.881E-02
0.001501   0.006627   0.012131
   73.000   3279.49  1.225E-02  2.712E-02  0.000E+00  3.937E-02
0.001623   0.006838   0.012137
   74.000   3283.59  1.221E-02  2.784E-02  0.000E+00  4.005E-02
0.001748   0.007059   0.012143
   75.000   3280.94  1.216E-02  2.806E-02  0.000E+00  4.022E-02
0.001875   0.007226   0.012150
   76.000   3275.22  1.218E-02  2.810E-02  0.000E+00  4.028E-02
0.002002   0.007405   0.012156
   77.000   3269.25  1.215E-02  2.820E-02  0.000E+00  4.035E-02
0.002130   0.007597   0.012163
   78.000   3262.70  1.208E-02  2.812E-02  0.000E+00  4.019E-02
0.002258   0.007801   0.012169
   79.000   3255.59  1.199E-02  2.805E-02  0.000E+00  4.004E-02
0.002386   0.008010   0.012176
   80.000   3247.91  1.198E-02  2.801E-02  0.000E+00  3.999E-02
0.002513   0.008166   0.012182
  100.000   2883.24  9.011E-03  1.807E-02  0.000E+00  2.708E-02
0.004627   0.011304   0.012290
  150.000   2135.41  4.750E-03  6.704E-03  0.000E+00  1.145E-02
0.007211   0.012421   0.012421
  200.000   1706.42  3.072E-03  2.607E-03  0.000E+00  5.679E-03
0.008194   0.012471   0.012471
  250.000   1434.58  2.141E-03  1.061E-03  0.000E+00  3.201E-03
0.008563   0.012490   0.012490
  300.000   1348.56  1.667E-03  8.282E-04  0.000E+00  2.495E-03
0.008770   0.012500   0.012500
  350.000   1354.46  1.479E-03  9.259E-04  0.000E+00  2.405E-03
0.008961   0.012510   0.012510
```

```
 400.000   1457.51  1.496E-03  1.486E-03  0.000E+00  2.982E-03
0.009218   0.012523   0.012523
 450.000   1769.08  1.832E-03  3.974E-03  0.000E+00  5.806E-03
0.009781   0.012552   0.012552
 500.000   2103.35  2.589E-03  8.634E-03  0.000E+00  1.122E-02
0.011117   0.012620   0.012620
 540.000   2252.39  3.154E-03  1.532E-02  0.000E+00  1.847E-02
0.013296   0.023260   0.024813
 541.000   2252.64  3.167E-03  1.547E-02  0.000E+00  1.864E-02
0.013366   0.023338   0.024816
 542.000   2253.31  3.179E-03  1.566E-02  0.000E+00  1.884E-02
0.013437   0.023417   0.024819
 543.000   2253.44  3.190E-03  1.583E-02  0.000E+00  1.902E-02
0.013508   0.023498   0.024823
 544.000   2253.30  3.202E-03  1.603E-02  0.000E+00  1.923E-02
0.013581   0.023580   0.024826
 545.000   2253.92  3.213E-03  1.631E-02  0.000E+00  1.952E-02
0.013654   0.023663   0.024830
 546.000   2253.48  3.224E-03  1.655E-02  0.000E+00  1.978E-02
0.013729   0.023748   0.024834
 547.000   2251.90  3.235E-03  1.684E-02  0.000E+00  2.007E-02
0.013805   0.023814   0.024837
 548.000   2249.89  3.246E-03  1.704E-02  0.000E+00  2.028E-02
0.013882   0.023881   0.024841
 549.000   2248.88  3.256E-03  1.730E-02  0.000E+00  2.055E-02
0.013960   0.023949   0.024845
 550.000   2246.77  3.266E-03  1.749E-02  0.000E+00  2.076E-02
0.014039   0.024019   0.024849
 600.000   1763.35  3.320E-03  1.949E-02  0.000E+00  2.281E-02
0.018704   0.025075   0.025075
 650.000   1273.27  2.542E-03  1.528E-02  0.000E+00  1.782E-02
0.022456   0.025257   0.025257
 700.000   1095.12  1.918E-03  1.744E-02  0.000E+00  1.935E-02
0.026119   0.028901   0.065337
 750.000    680.74  1.244E-03  0.000E+00  0.000E+00  1.244E-03
0.026120   0.028938   0.068456
 800.000    609.57  9.853E-04  0.000E+00  0.000E+00  9.853E-04
0.026120   0.028941   0.071536
 850.000    569.05  8.301E-04  0.000E+00  0.000E+00  8.301E-04
0.026120   0.028942   0.074617
 900.000    542.13  7.214E-04  0.000E+00  0.000E+00  7.214E-04
0.026120   0.028942   0.077749
 950.000    522.33  6.426E-04  0.000E+00  0.000E+00  6.426E-04
0.026120   0.028942   0.081051
1000.000    506.81  5.831E-04  0.000E+00  0.000E+00  5.831E-04
0.026120   0.028942   0.081127
1050.000    494.16  5.314E-04  0.000E+00  0.000E+00  5.314E-04
0.026120   0.028942   0.081127
1100.000    483.59  4.766E-04  0.000E+00  0.000E+00  4.766E-04
0.026120   0.028942   0.081127
1211.000    465.50  3.354E-04  0.000E+00  0.000E+00  3.354E-04
0.026120   0.028942   0.081127
```